Tech Science Press

Numerical Simulation Study on the Regularity of CIS Bedding Hydraulic Fracturing Based on 3D Penny-Shape Model

Jiangtao Li[1,2,*]

[1]School of Resources and Civil Engineering, Northeastern University, Shenyang, 110004, China
[2]CCTEG Shenyang Research Institute, Shenyang, 110016, China
[*]Corresponding Author: Jiangtao Li. Email: syccri@163.com

Abstract: In view of poor permeability of coal seam and soft coal quality in China's coal mining area, a point hydraulic fracturing method suitable for the occurrence characteristics of coal seam is put forward based on the characteristics of coal seam hydraulic fracturing and the field practical experience of coal seam hydraulic fracturing for many years. A theoretical and mathematical model of hydraulic fracturing is established. Based on the large-scale finite element software ABAQUS, numerical simulation of two dimensional and three dimensional hydraulic fracturing is carried out, and the fracture propagation law and its parameter sensitivity of coal seam point hydraulic fracturing are simulated and analyzed. The results show that when multi point synchronous hydraulic fracturing on the same layer borehole is carried out, there will be a certain coherence effect between fracture cracks when the interval between fracturing points is small. In the same fracturing time, the minimum effective stress in the coal body between the cracks will be reduced by about 10% when the gap between the cracks increase by 25%. We can use the fluctuation of effective stress field around fracture before and after fracturing as a discriminant index for effective radius of hydraulic fracturing. In general, it is advisable to have 10%~20% amplitude of effective stress field before and after fracturing.

Keywords: Coal seam permeability enhancement; gas extraction; hydraulic fracturing; numerical simulation

1 Introduction

In view of the complex geological conditions in China, coal seams in many mining areas are characterized by high gas content and low permeability, which is not conducive to gas extraction and utilization and disaster prevention. With the increase of coal mining depth, high probability of mining safety issues raise due to characteristics of high gas and low permeability [1,2]. Many technologies that can enhance the penetrability of coal seam are developed, such as hydraulic flushing in hole, deep-hole pre-splitting blasting and hydraulic slotting [3]. However, each technology has its adaptive conditions, and every technology is making better to overcome its disadvantages.

The hydraulic fracturing technology firstly used in oil and gas wells was successfully applied to improve production [4]. Remarkable consequences are achieved in the stimulation engineering of surface oil and gas wells with improved processes of hydraulic fracturing [5]. Due to similarity of the two industries, hydraulic fracturing technology has been gradually applied in the fields of coal and rock weakening, coal seam permeability enhancement and outburst prevention in underground mines [6–8]. But segmented hydraulic fracturing technology in underground coal mines is still under exploration [9–11]. By forming multiple fracturing zones caused by borehole sealing, the technology can reduce the impact of the original large fracture of the coal body near the borehole and increase the fracturing area. At the same time, the reduced fracturing space can save water injection, so it has a good application prospect.

2 Theoretical Model for Hydraulic Fracturing of Coal

2.1 Mathematical Model for Hydraulic Fracturing of Coal

In the process of hydraulic fracturing, the rock matrix is subjected to external forces such as water pressure, pore water pressure and ground stress. Considering the linear elastic constitutive relation of the deformation of the solid matrix, the following conclusions can be obtained:

$$\boldsymbol{\sigma} = \boldsymbol{D} : \boldsymbol{\varepsilon} \tag{1}$$

In the formula: $\boldsymbol{\sigma}$ is the total stress tensor, $\boldsymbol{D}$ is the elastic coefficient matrix, $\boldsymbol{\varepsilon}$ is a strain tensor related to displacement $\mathbf{u}$. Under the assumption of small deformation, $\boldsymbol{\varepsilon}$ satisfies the following formula:

$$\boldsymbol{\varepsilon} = \frac{1}{2}\left(\nabla \mathbf{u} + (\nabla \mathbf{u})^T\right) \tag{2}$$

The pore fluid in porous media satisfies the continuity equation of fluid. According to the divergence theory, the continuity equation at a certain point is expressed as [12]:

$$\frac{d}{dt}\left(\int_V \frac{\rho_w}{\rho_w^0} n dV\right) = -\int_S \frac{\rho_w}{\rho_w^0} n\boldsymbol{n} \cdot \mathbf{v}_w dS \tag{3}$$

In the formula, V is the integral domain, S is the surface of integral region, $\delta \boldsymbol{v}$ is the virtual velocity field vector, k is the effective permeability tensor of porous media, $\boldsymbol{n}$ is the cosine vector in the outer normal direction of a point on the boundary, $\mathbf{g}$ is the gravity acceleration vector, ρ_w is the fluid density, ρ_w^0 is the fluid reference density, n is the porosity, and $\mathbf{v}_w$ is the seepage velocity vector. The expression is [13]:

$$\mathbf{v}_w = -\frac{n^T}{n_w \mathbf{g} \rho_w} k\left(\frac{\partial p_w}{\partial \mathbf{x}} - \rho_w \mathbf{g}\right) \tag{4}$$

According to the principle of virtual work and the assumption of linear elastic deformation, the stress equilibrium equation in porous media can be obtained when the pore fluid is incompressible [14]:

$$\int_V \boldsymbol{\sigma} : \delta \boldsymbol{\varepsilon} \delta dV = \int_S \mathbf{t} \delta \boldsymbol{v} dS + \int_V \boldsymbol{f} \delta \boldsymbol{v} dV + \int_V n \rho_w \mathbf{g} \delta \boldsymbol{v} dV \tag{5}$$

In the formula, $\delta \varepsilon$ is the virtual deformation rate, $\mathbf{t}$ is the surface external force per unit area, $\boldsymbol{f}$ is the fluid fore per unit volume (excluding fluid gravity).

In the numerical simulation, the coupling Eq. (5) and the continuity Eq. (3) are solved by the ABAQUS software platform.

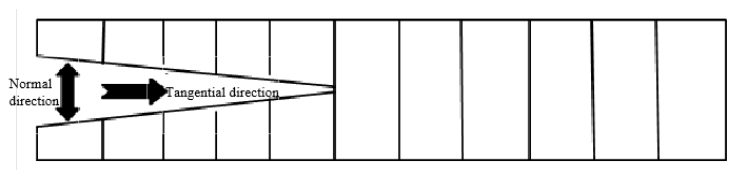There are normal flow and tangential flow in fluid in fracture in hydraulic fracturing, as shown in Fig. 1:

Figure 1: Schematic diagram of fluid flow in fractures

The seepage law of the unfractured rock mass is set as Darcy flow, while the fluid in the fracture is set as Newtonian fluid, and the flow law follows the pressure transfer formula of Newtonian fluid [15]:

$$Q = -k_t \nabla p \tag{6}$$

In the formula, Q is the fluid displacement in the fracture (m^3/s), k_t is the flow coefficient, which is related to crack width and fluid viscosity, and p is the fluid flow pressure (MPa).

According to Reynolds number equation, the fluid coefficient k_t can be expressed as:

$$k_t = \frac{d^3}{12\mu} \tag{7}$$

In the formula, d is the width of crack opening, m; μ is the viscosity coefficient of fracturing fluid, $Pa \cdot s$.

Fluid filtration is expressed as the fluid seepage velocity on the crack surface [16]:

$$\begin{cases} v_p = c_p(p_i - p_p) \\ v_b = c_b(p_i - p_b) \end{cases} \tag{8}$$

In the formula, v_p and v_b are respectively the fluid seepage velocity of upper and lower surfaces of the crack, p_i is the pore pressure of the introduced virtual node, which represents the internal pressure of the crack, p_p and p_b are respectively the pore pressure of the upper and lower surfaces of the crack, and c_p and c_b are respectively the filtration coefficient of upper and lower surfaces of the crack.

Suppose the rock mass cracking meets the traction separation rule [17]:

$$\mathbf{t} = \begin{Bmatrix} t_n \\ t_s \\ t_t \end{Bmatrix} = \begin{bmatrix} K_{nn} & 0 & 0 \\ 0 & K_{ss} & 0 \\ 0 & 0 & K_{tt} \end{bmatrix} \begin{Bmatrix} \delta_n \\ \delta_s \\ \delta_t \end{Bmatrix} = \mathbf{K}\boldsymbol{\delta} \tag{9}$$

In the formula, t is the traction vector, including normal vector t_n and two tangent vectors t_s and t_t, $\boldsymbol{\delta}$ is the separation displacement of rock mass, including normal vector δ_n and two tangential components δ_s and δ_t, $\mathbf{K}$ is the material stiffness matrix.

Crack propagation meets the maximum principal stress criterion, that is:

$$f = \left\{ \frac{\langle \sigma_{max} \rangle}{\sigma_{max}^0} \right\} \tag{10}$$

Among them, σ_{max}^0 is the critical maximum principal stress, and the symbol $\langle \rangle$ represents *Macaulay* bracket. The bracket is used to indicate that pure compression stress does not cause initial damage. When $f = 1$, cracking starts.

The failure mechanism of damage model includes two parts: The initial damage criterion and the law of damage evolution. Damage scalar D represents the average damage value between crack planes, and the initial value of damage scalar D is zero. When the damage model is established, D varies between [0,1], and when $D = 1$, the crack cracks completely.

The expressions of the normal and tangential stress components under the influence of damage are as follows [18]:

$$\begin{cases} t_n = (1-D)\overline{t_n} \\ t_s = (1-D)\overline{t_s} \quad (\overline{t_n} \geq 0) \\ t_t = (1-D)\overline{t_t} \end{cases} \tag{11}$$

In the formula, $\overline{t_n}$, $\overline{t_s}$ and $\overline{t_t}$ are respectively the predicted values of the stress components of the element under cracking. When $\overline{t_n} < 0$, $D = 0$. The expression of D is:

$$D = \delta_m^f (\delta_m^{\max} - \delta_m^0) / [\delta_m^{\max} (\delta_m^f - \delta_m^0)] \tag{12}$$

In the formula, $\delta_m^f = 2G_{eC} / T_e^0$. T_e^0 is the effective stress at initial time, δ_m^0 is the distance between upper and lower surfaces when cracks start to crack, $\delta_m^{\max}$ is the maximum value of the effective displacement between the upper and lower surfaces of the unit during loading, and G_{eC} is the equivalent critical fracture energy release rate, which is obtained from fracture energy release rate during fracture evolution.

In order to describe the interaction between tangential separation and normal separation, effective separation is used to represent:

$$\delta_m = \sqrt{\langle \delta_n \rangle^2 + \delta_s^2 + \delta_t^2} \tag{13}$$

In the formula, δ_m is the effective displacement value between the upper and lower surfaces of the unit during the loading process. δ_n, δ_s and δ_t are normal and two tangential displacement values respectively.

This paper adopts the damage evolution criterion of power law for the maximum principal stress extension criterion f. The power law expression is simple and has good convergence, so its expression is

$$\frac{G_e}{G_{eC}} = \left(\frac{G_I}{G_{IC}}\right)^{a_m} + \left(\frac{G_{II}}{G_{IIC}}\right)^{a_n} + \left(\frac{G_{III}}{G_{IIIC}}\right)^{a_o} \tag{14}$$

In the formula, G_{IC}, G_{IIC} and G_{IIIC} are respectively the type I, type II and type III critical fracture energy release rates, G_I, G_{II} and G_{III} are respectively the type I, type II and type III fracture energy release rates, and a_m, a_n, a_o and η are respectively the criterion material constants.

2.2 Extended Finite Element Format for Crack Propagation of Coal Hydraulic Fracturing

BASED on XFEM, the ABAQUS platform can simulate the crack propagation in complex stress field. The extended finite element approximation decomposes the displacement field into continuous and discontinuous parts, and its core formula is [19]:

$$u^h(x) = \sum_{I \in N} N_I u_I + \sum_{I \in N^{cr}} \bar{N} \left(H(\varphi(X)) - H(\varphi(x_I)) \right) a_I + \tag{15}$$
$$\sum_{I \in N^{tip}} \bar{N}_I \sum_{k=1}^{4} \left(F^k(x) - F^k(x_I) \right) b_I^k$$

Among them, N_I and $\bar{N}_I$ are the continuous partial shape function and discontinuous partial shape function respectively, N is the set of all nodes in the region, N^{cr} is the node set of crack through unit, N^{tip} is the crack tip node set, $H(\xi)$ is the *Heaviside* function, $\varphi(x)$ is the directed distance function, $F^k(x)$ is the tip enrichment function, u_I is the node degree of freedom, and a_I, b_I^k are degrees of freedom corresponding to enrichment functions.

The *Heaviside* enhancement function is activated when it passes through the unit, and its expression is:

$$H(x) = \begin{cases} 1 & x \geq 0 \\ -1 & x < 0 \end{cases} \tag{16}$$

For isotropic materials, based on linear elastic fracture mechanics, the expression of crack tip enhancement function is:

$$\{F_l(r,\theta)\}_{l=1}^4 = \left\{\sqrt{r}\sin\frac{\theta}{2}, \sqrt{r}\cos\frac{\theta}{2}, \sqrt{r}\sin\theta\sin\frac{\theta}{2}, \sqrt{r}\sin\theta\cos\frac{\theta}{2}\right\} \tag{17}$$

In the formula, (r,θ) is Gauss's point x coordinates in the polar coordinates system of the crack tip.

ABAQUS platform can put formula (15) into formula (5) for numerical discretization to obtain the equilibrium equation, and then the relative stress and displacement fields of crack propagation can be obtained by iteration.

3 Validation of Simulation of Crack Propagation in Abaqus Hydraulic Fracturing

3.1 Three Dimensional Penny-Shape Model for Crack Propagation in Hydraulic Fracturing

Hydraulic fracturing began in the United States in the 1940s and has been developed for decades. Its theoretical research has been quite mature. The most common hydraulic fracturing mathematical models are the PKN model of plane strain and the three-dimensional Penny-Shape model [20], and the initial analytical expressions are given. In the 1980s, some scholars found that there was a fluid lag region near the crack tip [21]. Savitski improved the traditional analytical expression of hydraulic fracturing according to different control parameters and gave the asymptotic solution of Penny-Shape model [22]. This paper, based on the asymptotic solution with toughness as the control parameter, analyzes the rationality of numerical simulation results of fracturing fracture based on XFEM.

The Penny-Shape model is a cylinder with a radius of 45 m and a height of 30 m. There is a borehole in the center with a diameter of 0.01 m. The elastic modulus is 17 GPa, Poisson's ratio is 0.2, initial porosity is 0.2, permeability coefficient is 9.8×10^{-9} m/s, fluid viscosity is 1×10^{-3} Pa·s, injection displacement is 0.001 m³/s, initial saturation is 1.0, initial pore pressure is 0, initial ground stress is 0, and fracture energy release rate is 120 N/m. The three-dimensional Penny-Shape model is established as shown in Fig. 2.
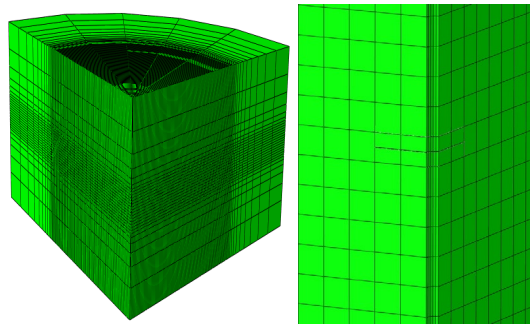

Figure 2: Grid sketch of 3D Penny-Shape model

3.2 Analysis of Numerical Simulation Results of Classical Hydraulic Fracturing Models

The progressive solution of Penny-Shape model with viscosity control is as follows: Crack length:

$$L = \left(\frac{9}{2\pi^2}\right)^{1/5}\left(\frac{E'Q_0}{K'}\right)^{2/5} t^{2/5} \tag{18}$$

Crack width:

$$w = \left(\frac{3}{8\pi}\right)^{1/5} Q_0^{1/5}\left(\frac{K'}{E'}\right)^{4/5} t^{1/5} \tag{19}$$

Crack entrance pressure:

$$p = 0.3004\left(K'\right)^{6/5}\left(Q_0 E'\right)^{-1/5} t^{-1/5} + S \tag{20}$$

In the formula $E' = \dfrac{E}{1-v^2}$, E is the modulus of elasticity, v is the Poisson ratio, and $K_{IC} = \sqrt{G_c \dfrac{E}{1-v^2}}$ is what in the formula $K' = 4\left(\dfrac{2}{\pi}\right)^{1/2} K_{IC}$. G_c is fracture energy release rate, Q_0 is injection displacement, t is fracturing time, and S is principal stress perpendicular to fracture propagation direction. The fracturing duration of the Penny-Shape model simulation is 40s, and the simulation results are shown in Fig. 3.
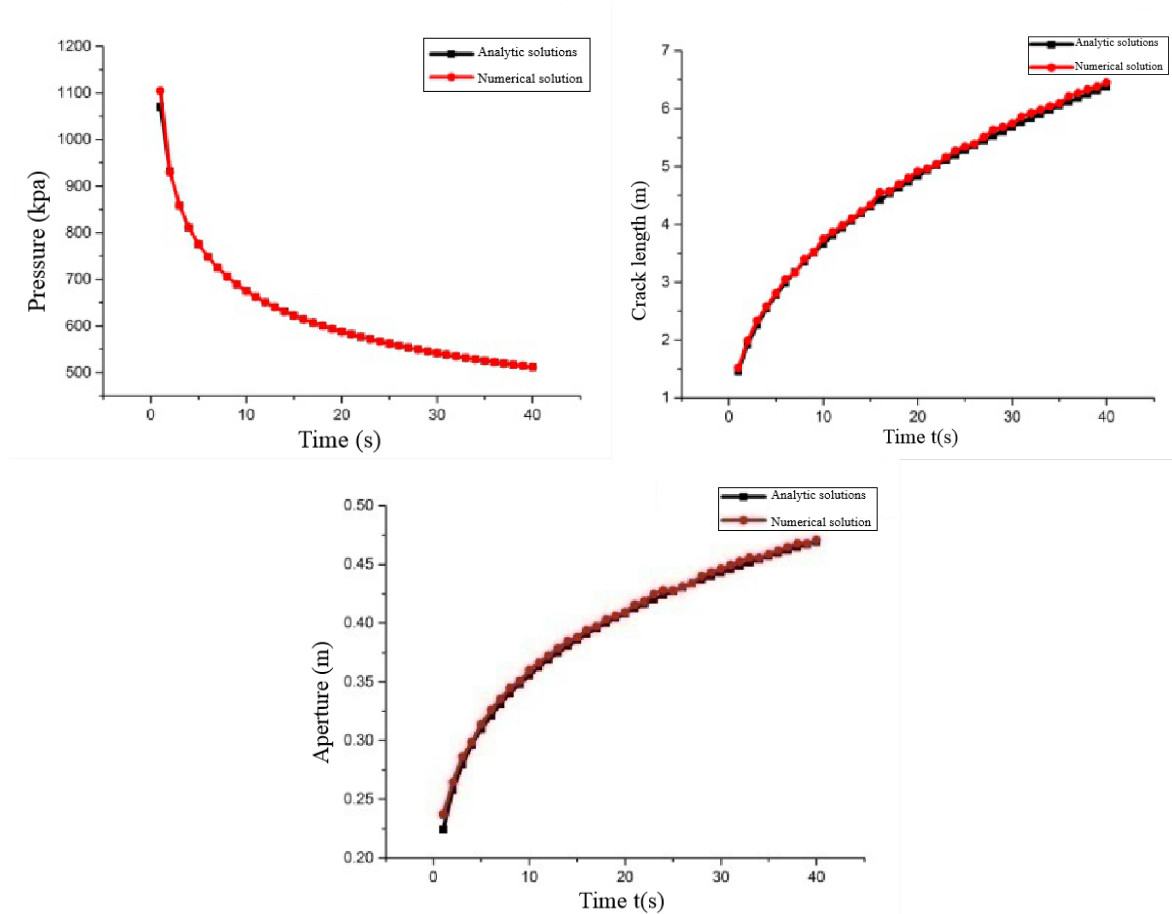

Figure 3: Comparison between numerical solution and analytical solution of Penny-Shape model

From the comparison between the numerical solution and the analytical solution in Fig. 3, it can be seen that the numerical solution is basically consistent with the analytical solution in both the KGD model and the Penny-Shape model, and the error is no more than 1%. For example, when t = 40 s in Penny-Shape model, the numerical solution of crack length L = 6.45 m, the analytical solution of crack length L = 6.38 m, and the error = [(6.43 – 6.38)/6.38] × 100% = 0.78%. Therefore, the results obtained by using ABAQUS extended finite element method to simulate the hydraulic fracturing in actual engineering has high reliability.

4 Simulation Analysis of Coal Seam Bedding Hydraulic Fracturing Based on 3D Penny-Shape Model

Based on the theoretical and mathematical model of hydraulic fracturing established above, a three-dimensional Penny-Shape model of coal body hydraulic fracturing bedding borehole was established to study the three-dimensional propagation behavior and law of hydraulic fractures. All sides of the model were normal constraints, and the simulated buried depth of the coal seam was 600 m. The lateral pressure coefficients perpendicular to the crack propagation direction were 1.0, and the lateral pressure coefficients in the other two directions were 1.5. The basic parameters of the simulated coal seam were as follows: the elastic modulus was 1.0 GPa, Poisson ratio was 0.3, tensile strength was 0.28 MPa, fracture energy release

rate was 100 N/m, fluid viscosity was 1×10^{-6} kPa·s, permeability coefficient was 1×10^{-12} m/s, fluid filtration coefficient was 1×10^{-12} m/(kPa.s), initial pore pressure was 100 kPa, initial saturation was 1.0, and pore ratio was 0.25.

4.1 Analysis of Fracture Propagation Law of Single Point Segmented Hydraulic Fracturing of Bedding Borehole

The hydraulic fracturing model of bedding borehole was established, in which the borehole with diameter of 80 mm passed through the whole model and was located in the center of the simulated coal seam thickness direction. The injection displacement of 0.5 L/s was continuously injected into the low permeability coal seam by the fracturing hole to carry out the fracturing, and the fracturing time was 900s. Based on the model, the crack initiation and propagation of hydraulic fractures of single-point fracturing along bedding were studied, which provided a basis for the study of fracture propagation law of multi-point hydraulic fracturing.

The fracturing mouth pressure-time curve given in Fig. 4 shows that the fracturing mouth pressure-time curve of the bedding borehole hydraulic fracturing is similar to the cross-layer borehole pressure-time curve. They all have three stages: Near-linear pressure rising stage, nonlinear fast drop stage and stable extended stable pressure stage. The crack initiation pressure is about 75 MPa, and the stable propagation pressure is close to the stress of primary rock. The variation curve of fracturing mouth opening with time given in Fig. 5 shows that the opening of bedding borehole fracturing mouth shows a straight line of nearly 90°, increasing sharply from zero to about half of the maximum opening of the whole fracturing mouth at the beginning of fracturing, and then increases slowly until the maximum opening is reached at the end of fracturing. The maximum of fracturing mouth is about 35 mm. Compared with the fracturing mouth pressure-time curve and opening curve of cross-layer single borehole fracture, the difference of crack initiation pressure of fracturing mouth is about 1 MPa, which is caused by different injection displacement. When the injection displacement decreases, the crack initiation pressure will decrease.

Fig. 6 shows the circumferential stress cloud map in the direction perpendicular to the fracture propagation at the end of fracturing. It can be clearly seen that there are obvious circumferential stress increasing areas on both sides of the fracture surface. Fig. 7 shows the distribution cloud map of pore pressure near the fracture at the end of fracturing. It can be seen intuitively that the pore pressure on both sides of the fracture surface has obvious pressure gradient change. As the distance from the fracture surface increases, the pore pressure decreases gradually until it reaches the initial pore pressure. The reason why the distribution law of pore pressure is different from the distribution of pore pressure of cross-layer borehole hydraulic fracturing is that the lithology of coal body on both sides of hydraulic fracturing fracture in bedding boreholes is consistent, and the pore pressure is not limited, that is, because of the permeability and filtration of fracturing fluid on the fracture surface, the fracturing fluid in coal on both sides of the fracture surface increases, so the pore pressure near the both sides of fracture surface becomes larger. However, the lithology of roof and floor is different from that of coal seam in cross-layer borehole hydraulic fracturing, and the permeability of roof and floor is slightly lower than that of coal seam. Therefore, when fracturing fluid enters coal body and seeps into roof and floor direction, it will be restricted by roof and floor, which makes fracturing fluid accumulate in the only thickness direction of coal seam, so the pore pressure field formed is different from the pore pressure field formed by bedding borehole fracturing.

Fig. 8 shows the effective stress curves on three horizontal paths at the end of fracturing, and the origin of coordinates is located on the fracture surface. Horizontal path 1 is composed of a series of points on the line at 0.1 m from the borehole axis along the direction perpendicular to the crack propagation. Horizontal path 2 is composed of a series of points on the line parallel to horizontal path 1 and at 0.4 m from the borehole axis. Horizontal path 3 is composed of a series of points on the line parallel to horizontal path 1 and at 1 m from the borehole axis. It can be seen intuitively that when moving away from the fracture surface along the borehole axis, the effective stress on different paths gradually nonlinearly decreases to a sable value. The stable value is basically the same as that of the original rock stress field.
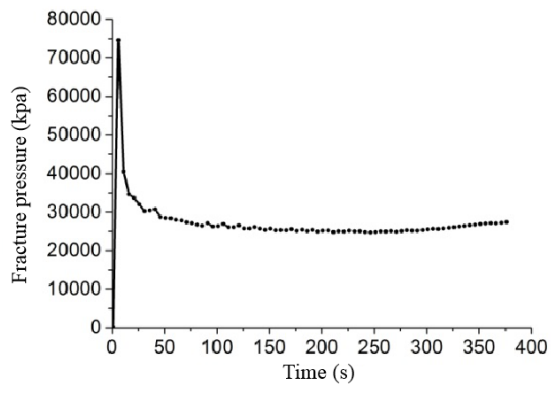
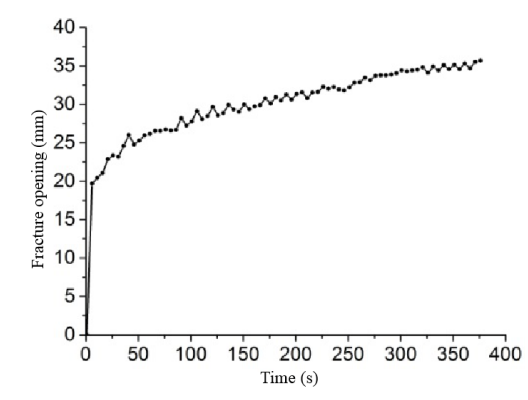**Figure 4:** Fracturing mouth pressure-time curve

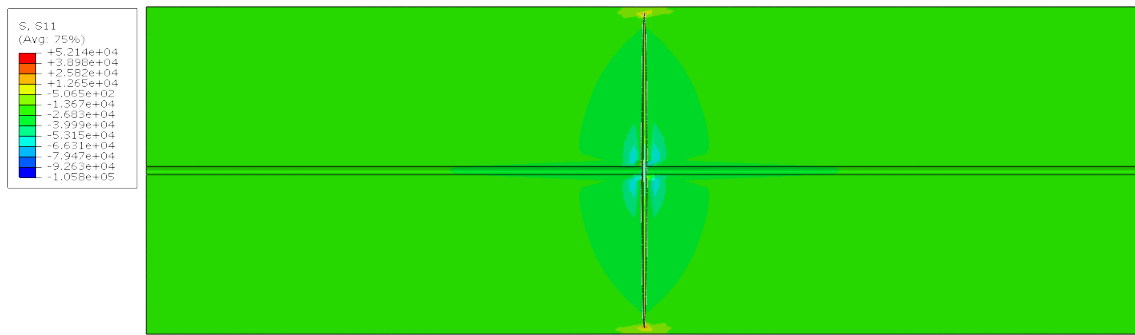**Figure 5:** Fracturing mouth opening-time curve

Figure 6: Circumferential stress in the direction perpendicular to the fracture propagation at the end of fracturing (unit: kPa)
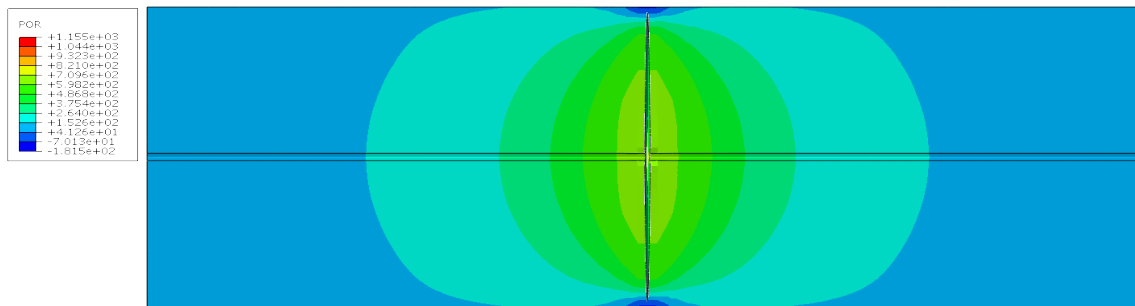

Figure 7: Pore pressure near fracture at the end of fracturing (unit: kPa)
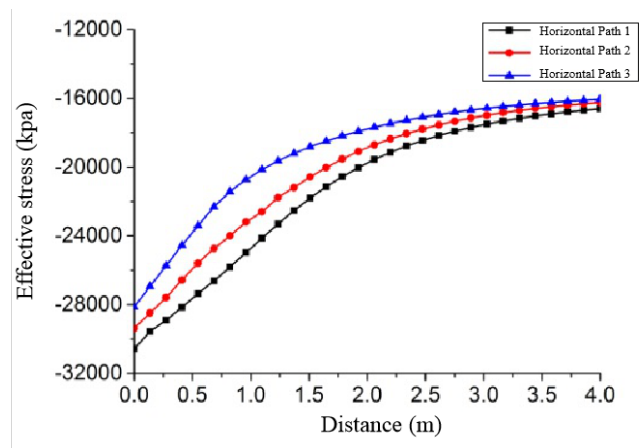
Figure 8: Effective stress curve of horizontal path

4.2 Analysis of Crack Propagation Law of Multi-Point Segmented Hydraulic Fracturing of Bedding Borehole

According to the numerical simulation results of single-point fracturing in 3.1, the spacing of multi-point fracturing is 4 m and 5 m, and the crack propagation law of bedding multi-point fracturing is analyzed. The location of fracturing points is as follows:
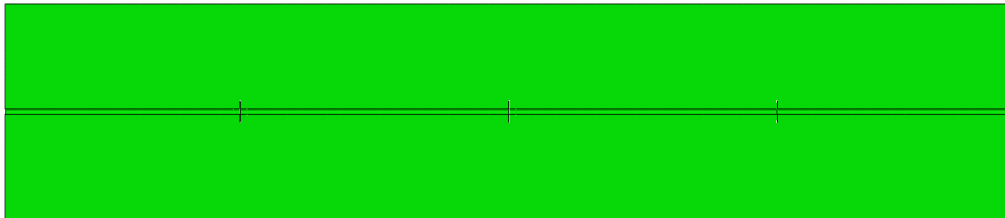
Figure 9: Distribution of fracturing points

(1) Stress field analysis of point fracturing with 4 m spacing

According to the fracture point position given in Fig. 9, the intermediate fracture is defined as the fracture in the middle of Fig. 9, the left fracture is the one on the left side of the intermediate fracture, and the right fracture is the one on the right side of the intermediate fracture. According the fracturing mouth pressure-time curves of three fractures produced by three-point fracturing and the fracture produced by single-point fracturing in Fig. 10, it can be seen that the crack initiation pressures of all fractures are the same, and the stable propagation pressures of the three fractures produced by three-point fracturing are basically the same, but the stable propagation pressures of three fractures produced by three-point fracturing are all larger than that of single-point fracturing. The reason is that when hydraulic fractures produce opening displacement under the condition of three-point fracturing, the coal body between the fractures is compressed and deformed, so that when the intermediate fracture expands and produces transverse deformation, they are restricted by fracturing fractures on both sides. However, this effect is mutual, that is, the lateral displacement caused by fracturing crack propagation on both sides is also affected by the crack propagation of intermediate fracturing. Therefore, the stress field is increased because of the influence of the fracture propagation on coal between fractures during the stable propagation stage of three fractures. Therefore, larger stable propagation pressure is needed to maintain further propagation of cracks.

From the opening-time curves of fracturing mouth of three fractures produced by three-point fracturing and the fracture produced by single-point fracturing in Fig. 11, it can be seen that, at the beginning of fracturing, the opening degree of the fracturing mouth increases rapidly and then increases slowly until the end of fracturing. However, three fractures produced by three-point fracturing have larger opening than

single point fracturing. The reason is that two sides of the coal body between the fractures are simultaneously pressured by the high-pressure fracturing fluid in the two hydraulic fractures, so the compression degree of the coal body is larger than that of the coal body on both sides of the fracture surface when single-point fracturing. As a result, the opening of three fractures produced by three-point fracturing will increase at the same fracturing time.

Fig. 12 shows the circumferential stress cloud map in the direction perpendicular to the fracture propagation at the end of the fracturing. It can be clearly seen that there is an fracturing increasing area of circumferential stress on both sides of each fracture surface perpendicular to the fracture propagation, especially the superposition of the increasing area of circumferential stress in the intermediate fracture and the increasing area of circumferential stress in fractures on both sides, forming a new fracturing increased area. From the above, there is a significant interaction between fractures when the fracturing point is set with spacing of 4 m. Fig. 13 shows the distribution cloud map of pore pressure near the fracture at the end of fracturing. It can be seen intuitively that there is a significant pore pressure gradient change on both sides of the fracture surface, and the pore pressure field strength in the coal body between fractures is higher than that in the other coal bodies. The content of fracturing fluid between fractures is higher than that in other coal bodies, so the pore pressure will naturally be larger.

Fig. 14 shows the effective stress curves on the three horizontal paths in 3.1, where the origin of coordinates is on the fracture surface of the intermediate fracture. It can be seen from the figure that the effective stress field of the coal body between fractures nonlinearly decreases to the minimum value with the increase of the distance from the cracks, and the minimum value is located in the middle of the two cracks, that is, the distance from any fracture surface is 2 m. From the figure, it can be seen that the effective stress of the horizontal path 1, the horizontal path 2 and the horizontal path 3 gradually decreases. The minimum effective stress is about 23 MPa on the horizontal path 3, which is about 20% higher than the effective stress at the same position on the horizontal path 3 in 3.1. The reason is that the coal between fractures is affected by the high pressure fracturing fluid of the fractures on both sides, which makes the coal solid skeleton suffer greater compression deformation, and the circumferential stress increases correspondingly. Although the pore pressure in the coal between fractures will also increase, the increase is much less than that of circumferential stress, so the effective stress will increase.
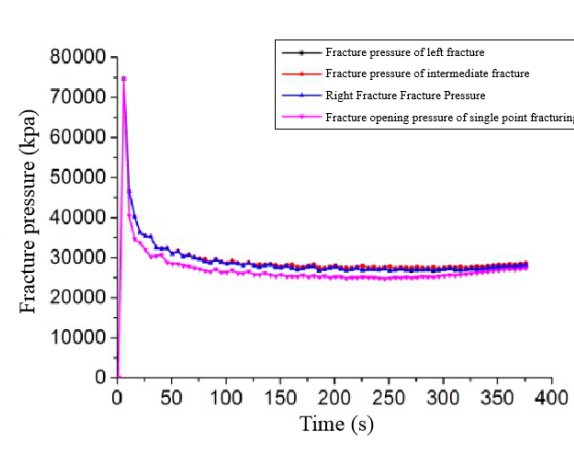

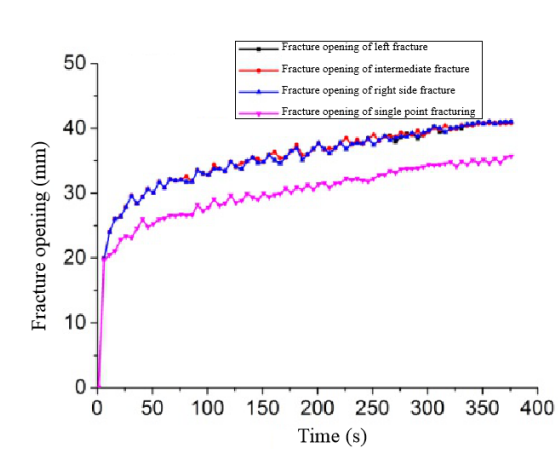**Figure 10:** Pressure-time curve of fracturing mouth

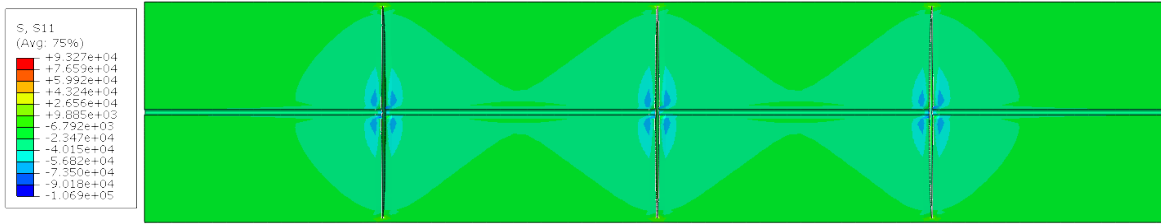**Figure 11:** Opening-time curve of fracturing mouth

Figure 12: Circumferential stress perpendicular to the direction of fracture propagation at the end of fracturing (unit: kPa)
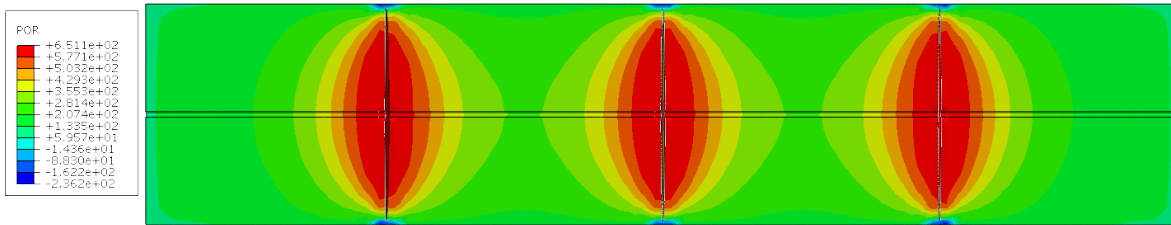

Figure 13: Pore pressure near fracture at the end of fracturing (unit: kPa)
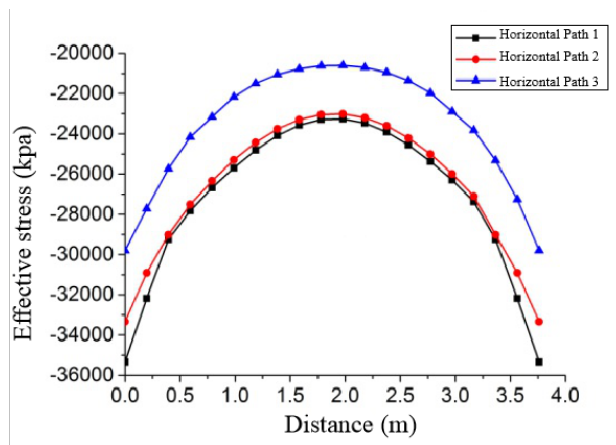

Figure 14: Effective stress curve of horizontal path

(2) Stress field analysis of point fracturing with 5 m spacing

From the fracturing mouth pressure-time curves of three fractures produced by three-point fracturing and the fracture produced by single-point fracturing in Fig. 15, it can be seen that the fracturing mouth pressure-time curves of fractures with 5 m interval between fracturing points has the same change rule with the fracturing mouth pressure-time curves of fractures with 4 m interval between fracturing points. The crack initiation pressure is about 75 MPa, and the stable propagation pressure of three fractures produced by three-point fracturing is higher than that of the single-point fracturing under the condition of 5 m fracture spacing. The reason is consistent with the working condition with the fracture spacing of 4 m. From the variation curves of fracturing mouth opening with time of three fractures produced by three-point fracturing and the fracture produced by single-point fracturing with the fracturing spacing of 5 m in Fig. 16, it can be seen that the fracturing mouth opening of three fractures with 5 m spacing is higher than that of the single-point fracturing, and the reason is consistent with the working condition with the fracture spacing of 4m. Fig. 17 and Fig. 18 respectively show the fracturing mouth pressure-time curves of the intermediate fracture and the variation curves of opening with time with 5 m and 4 m spacing. It can be seen intuitively that the

variation laws of fracturing mouth pressure and opening with time are basically consistent when the fracture spacing is 5 m and 4 m.

Fig. 19 shows the circumferential stress cloud map perpendicular to the direction of fracture propagation at the end of fracturing. It can be clearly seen that there are more obvious circumferential stress increasing zones on both sides of the fracture surface. Fig. 20 shows the distribution cloud map of pore pressure near the fracture at the end of fracturing. It can also be seen intuitively that there is a significant pore pressure gradient change on both sides of the fracture surface. Comparing with the distribution of pore pressure when the fracture spacing is 4 m, it can be seen that the pore pressure between the fractures decreases slightly according to the gradient change range. This is because the distance between fractures has increased. At the same time, the amount of fracturing fluid permeability and filtration to the same lithology of low permeability coal is basically the same, but the volume of coal between fractures increases. The larger volume of coal is filled with the same quality fracturing fluid, so the pore pressure will naturally decline.

Fig. 21 shows the effective stress curves on the three horizontal paths described in 3.1, where the coordinate origin is located on the intermediate fracture surface. It can be seen from the figure that with the increase of the distance from the fracture surface, the effective stress on any path is gradually reduced to the minimum value, which is consistent with the reason when the fracture spacing is 4 m. In addition, the minimum values of the effective stress on paths 1, 2 and 3 are about 21 MPa, 20 MPa and 19 MPa, respectively. These minimum values of the effective stress are smaller than the minimum values of the effective stress on horizontal paths with 4 m fracture spacing. Taking the effective stress on the horizontal path 2 as an example, as shown in Fig. 22, the variation trend of the effective stress on the horizontal path is symmetrical and decreases at first and then increases, whether the fracture spacing is 5 m or 4 m. It can be seen intuitively from the figure that the minimum effective stress with 5 m fracture spacing is less than the minimum effective stress with 4 m fracture spacing. The reason is that the fracture spacing increases, and the volume of coal between fractures increases. In the same fracturing time, the fracturing fluid in the fracture does the same work to the coal body between fractures, so the compression degree of the coal body between fractures will be weakened, and the stress increment in the coal body will be reduced, so the minimum effective stress is closer to the original rock stress.
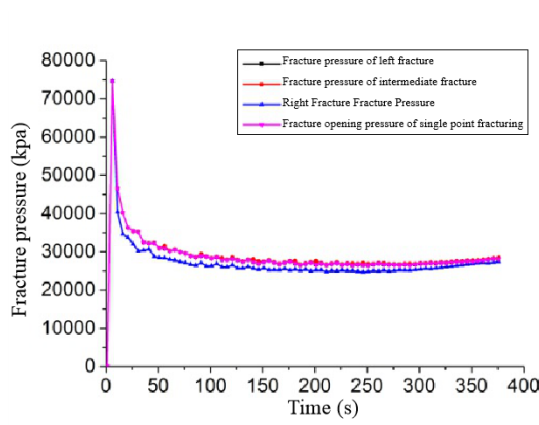

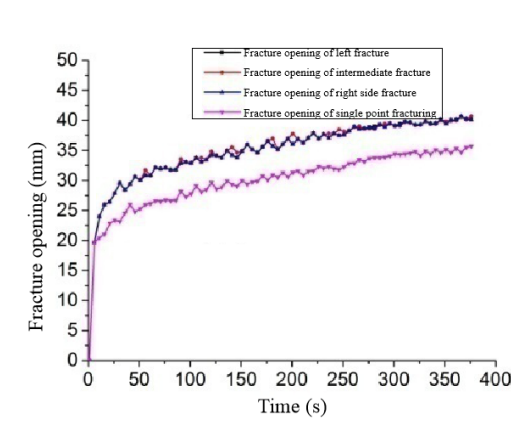**Figure 15:** Fracturing mouth pressure-time curves

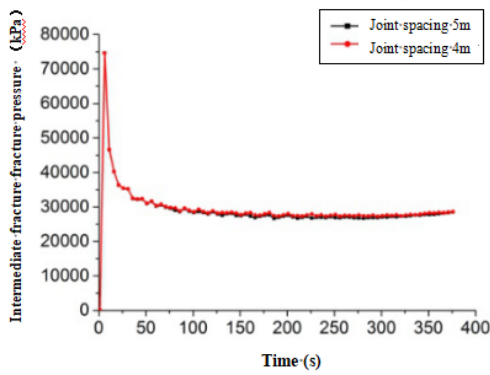**Figure 16:** Fracturing mouth opening-time curves

Figure 17: Fracturing mouth pressure-time curves of the intermediate fracture
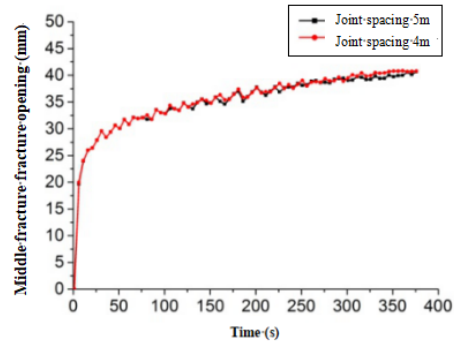
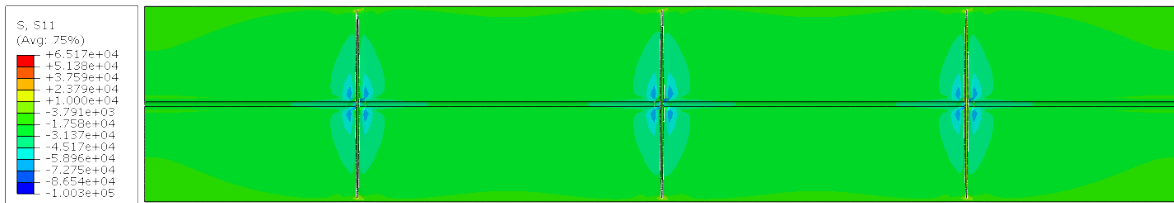**Figure 18:** Fracturing mouth opening-time curves of the intermediate fracture

Figure 19: Circumferential stress perpendicular to the direction of fracture propagation at the end of fracturing (unit: kPa)
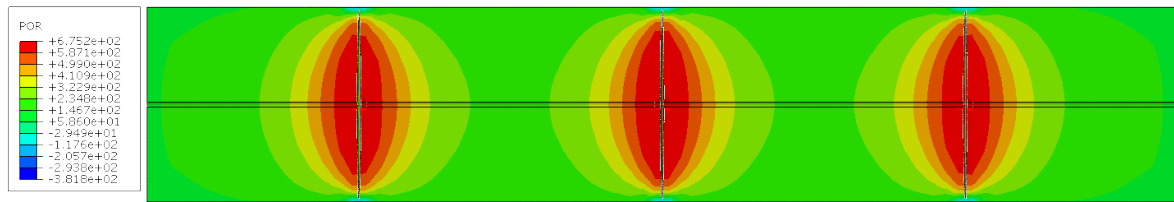

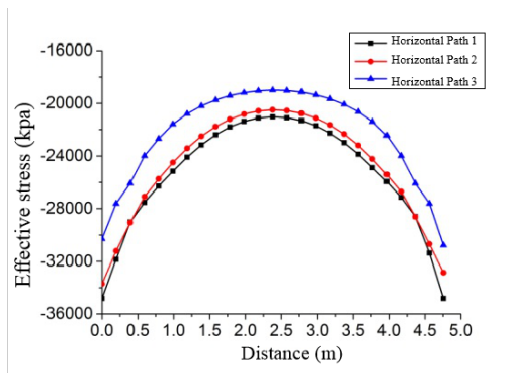**Figure 20:** Pore pressure near fracture at the end of fracturing (unit: kPa)

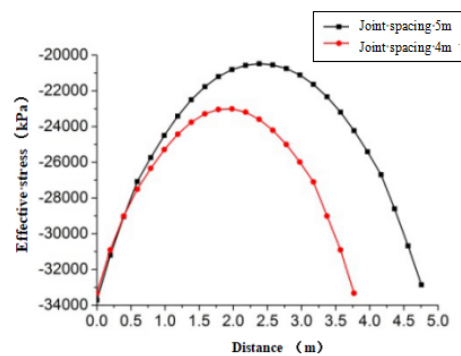**Figure 21:** Effective stress curves of the horizontal path

Figure 22: Effective stress curves of the horizontal path 2

5 Conclusions

(1) Based on linear elastic fracture mechanics and fluid-solid coupling theory, a theoretical model of fracture propagation of hydraulic fracturing in coal is established. The finite element discretization scheme of the coupled model and the extended finite element scheme of crack propagation solution are derived. Compared with the cohesive force method and virtual fracture closure method commonly used in hydraulic fracturing fracture propagation simulation, the extended finite element method can not only consider the seepage failure of fracturing fluid, but also truly simulate the fracture propagation process according to the stress state of coal body at all times.

(2) Compared with the analytical solution of the classical Penny-Shape model of hydraulic fracturing, it found that the theoretical model of hydraulic fracturing and the extended finite element numerical simulation results are completely consistent with the corresponding classical model, which verifies the validity and accuracy of the theoretical model and the extended finite element method in simulating the fracture propagation of hydraulic fracturing.

(3) Hydraulic fracturing simulation results of bedding boreholes based on three-dimensional model show that when multi-point synchronous hydraulic fracturing is conducted on the same bedding borehole, when the spacing between fracturing points is small, there will be some coherent effects between fracturing fractures. In the same fracturing time, when the fracture spacing increases by 25%, the minimum effective stress in the coal body between the fractures will be reduced by about 10%. The fluctuation of the effective stress field around the fracture before and after fracturing can be used as the criterion of the effective influence radius of hydraulic fracturing. Generally speaking, 10%~20% fluctuation amplitude of the effective stress field before and after fracturing can be taken.

Conflicts of Interest: The authors declare that they have no conflicts of interest to report regarding the present study.

References

[1] L. Yuan, "Key technique of safe mining in low permeability and methane-rich seam group," *Chinese Journal of Rock Mechanics and Engineering*, vol. 27, no. 7, pp. 1370–1379, 2008.

[2] L. Yuan, "Strategic consideration of deep coal and gas co-mining in China," *Journal of China Coal Society*, vol. 41, no. 1, pp. 1–6, 2016.

[3] X. Li, C. Zhai and Q. Li, "Research and application of coal seam pulse hydraulic fracturing technology," *Journal of China Coal Society*, vol. 36, no. 12, pp. 1996–2001, 2011.

[4] Y. Duan, S. Yang, M. Zhang, Z. Tan and G. Zhang, "Research and application of the multipoint control hydraulic fracturing technology for improving permeability and rapidly eliminating outburst," *Journal of Safety and Environment*, vol. 15, no. 6, pp. 39–44, 2015.

[5] H. Yang, "Underground segmentation point hydraulic fracturing antireflection for low-permeability coal seams," *Journal of University of Science & Technology Beijing,* vol. 34, no. 11, pp. 1235–1239, 2012.

[6] B. Lin, Z. Li, C. Zhai, Q. Bi and Y. Wen, "Pressure relief and permeability-increasing technology based on high pressure pulsatin hydraulic fracturing and its application," *Journal of Mining and Safety Engineering*, vol. 28, no. 3, pp. 452–455, 2011.

[7] Q. Cheng, B. Huang, C. Liu, M. Wei, J. Fu *et al.,* "Hydraulic fracturing theory of coal-rock mass and its technical framework," *Journal of Mining and Safety Engineering*, vol. 28, no. 2, pp. 167–173, 2011.

[8] S. Tang, Z. Yan and B. Zhu, "Effect of crustal stress on hydraulic fracturing in coalbed methane wells," *Journal of China Coal Society*, vol. 36, no. 1, pp. 65–69, 2011.

[9] P. A. Martynyuk, "Features of hydraulic fracture growth in the compression field," *Journal of Mining Science*, vol. 44, no. 6, pp. 544–553, 2008.

[10] X. Fu, "Study of underground point hydraulic fracturing increased permeability technology," *Journal of China Coal Society*, vol. 36, no. 8, pp. 1317–1321, 2011.

[11] K. Wang, X. Fu, Y. Wang, J. Li, J. Zhang *et al.*, "Patent: Segmental hydraulic fracturing coal seam pressure releasing device and method.No.102704905a. beijing," State Intellectual Property Office, 2012.

[12] Z. Zhang, Q. Shi and D. Yan, "Establishment and application of fixture constraint models in finite element analysis of welding process" *Acta Metallurgica Sinica*, vol. 46, no. 2, pp. 189-194, 2010.

[13] P. Dong and X. Xu, "Mathematical model of reservoir fluid solid coupling and its finite element equation," *Acta Petrolei Sinica*, vol. 19, no. 1, pp. 64–70, 1998.

[14] Z. Lian, H. Wu and J. Zhang, "Fluid solid coupling numerical simulation of hydraulic fracturing expansion," *Rock and Soil Mechanics*, vol. 29, no. 11, pp. 3021–3026, 2008.

[15] H. Wu, B. Xue, G. Zhang and X. Wang, "Three-dimensional numerical simulation of hydraulic fracturing in oil wells," *Journal of University of Science and Technology of China*, vol. 38, no. 15, pp. 1323–1325, 2008.

[16] J. Hagoort, A. Settari, D. B. Weatherill, "Modeling the propagation of water flood-induced hydraulic fractures," *Society of Petroleum Engineers Journal*, vol. 20, no. 4, pp. 293-303, 1980.

[17] T. Li, K. Sun and S. Zhang, "Study on fracture expansion law of hydraulic fracturing in transversely isotropic oil and gas reservoirs," *Chinese Journal of Computational Mechanics*, vol. 33, no. 5, pp. 767–772, 2016.

[18] B. Sobhaniaragh, W. J. Mansur and F. C. Peters, "Three-dimensional investigation of multiple stage hydraulic fracturing in unconventional reservoirs," *Journal of Petroleum Science & Engineering*, vol. 146, no. 10, pp. 1063–1078, 2016.

[19] J. H. Song, P. M. A. Areias and T. Belytschko, "A method for dynamic crack and shear band propagation with phantom nodes," *International Journal for Numerical Methods in Engineering*, vol. 67, no. 6, pp. 868–893, 2006.

[20] T. K. Perkins and L. R. Kern, "Widths of hydraulic fractures," *Journal of Petroleum Technology*, vol. 13, no. 9, pp. 369–390, 1961.

[21] J. Desroches, "Crack tip region in hydraulic fracturing," *Proceedings of the Royal Society A*, vol. 447, no. 1929, pp. 39–48, 1994.

[22] A. A. Savitski and E. Detournay, "Propagation of a penny-shaped fluid-driven fracture in an impermeable rock," *Asymptotic Solutions. International Journal of Solids & Structures*, vol. 39, no. 26, pp. 6311–6337, 2002.